This is an Accepted Manuscript of an article published by Taylor & Francis in Philosophical Magazine, Volume 99, 2019 – Issue 13, available online: https://doi.org/10.1080/14786435.2019.1587183

# Thermo-kinetic behavior of $Ge_{20}Te_{75}I_5$ glass for infrared optics

Daniela Brandová*, Roman Svoboda

*University of Pardubice, Faculty of Chemical Technology, Department of Physical Chemistry, Studentska 573, 532 10 Pardubice, Czech Republic.*

## Abstract

The iodine-doped $GeTe_4$ infrared chalcogenide glass was studied by means of differential scanning calorimetry DSC, X-ray diffraction XRD, Raman spectroscopy and infrared microscopy. Extensive non-isothermal thermo-kinetic characterization of the glass transition, crystallization and melting phenomena was performed in dependence on the particle size. The Tool–Narayanaswamy–Moynihan model was applied to describe the enthalpy relaxation processes: the compositional evolution of the relaxation parameters was then explained in terms of the structural changes and movements of the characteristic structural units. Mathematic deconvolution was applied to treat the complex crystallization kinetics – two crystal growth sub-processes were identified and described in terms of the autocatalytic Šesták-Berggren model. Based on the XRD and microscopic analyses the following crystallization mechanisms were revealed: initial precipitation of tellurium (surface-located) followed by a combined surface- and bulk-located formation of GeTe and $GeI_4$ phases. Based on the DSC results obtained for fine powders, presence of mechanically induced defects was found to accelerate the Te precipitation, the consequences of which are discussed with regard to the performance of nowadays glass stability criteria.

Keywords: Ge-Te-I glasses, thermal behavior, glass transition, crystallization kinetics, glass stability

* Corresponding author: Tel.: +420 466 037 346; E-mail address: daniela.brandova@upce.cz

## 1. Introduction

Tellurium-based chalcogenide glasses belong to promising materials with applicability in the far-infrared (far-IR) optics. [1,2] These materials were found to be suitable for applications such as far-infrared biosensing [3], $CO_2$ detection at 15 μm [4], or IR optics focused on outer space detection of the biological life markers (e.g. $CO_2$, $H_2O$, $O_3$ absorption bands) [5,6]. The great advantage of Te-based glasses is their large transmittance range in IR optical region (up to 20 μm [4,7]), which depends on the exact composition of particular chalcogenide material. Nonetheless, the strong tendency towards crystallization and low glass stability are the main disadvantages associated with the purely tellurium-based chalcogenide glasses. These issues can be solved by doping the telluride matrix with e.g. selenium, gallium or iodine. [7-9] Recently, several studies reported on thermal behavior of Ga- and Se-doped Ge-Te glasses. [10-18] The Ga-doped materials were in certain cases found to manifest relatively high tendency towards crystallization, which may complicate potential applicability in the fiber-drawing or lens-molding industry. The Se-doped Ge-Te materials, on the other hand, can exhibit lower transmittance or a narrower transmittance window due to the presence of selenium. [16,17] Regarding the doping by iodine, only very few (rather qualitative) results can be found in literature [4,9,18]. The addition of iodine into the Ge-Te glassy matrix causes disruption of the three-dimensional network and the subsequent improvement of the thermal properties; the volatility of iodine may however make the synthesis of the glassy material more difficult. [4,9,18]

In the present paper, the detailed results from the thermal and structural analysis of $Ge_{20}Te_{75}I_5$ chalcogenide glass will be reported. Differential scanning calorimetry (DSC) will be used to gain the information about the structural relaxation and crystallization processes under non-isothermal conditions and in dependence on particle size. The thermo-kinetic behavior will be explained based on the structural information provided by X-ray diffraction

(XRD), Raman spectroscopy and infrared microscopy. In addition to the kinetic data, the glass stability (GS) criterion will be evaluated in dependence on experimental conditions; the impact and reliability of these types of evaluations for the potential real-life far-IR optics applications will be discussed.

## 2. Theory

### 2.1 Structural relaxation

The phenomenological Tool-Narayanaswamy-Moynihan (TNM) [19-21] model is often used to describe the structural relaxation kinetics in the vicinity of glass transition; this model is defined as:

$$F(t) = \exp\left[-\left(\int_0^t \frac{dt}{\tau(T,T_f)}\right)^{\beta}\right] \tag{1}$$

$$\tau(T,T_f) = A_{TNM} \cdot \exp\left[x\frac{\Delta h^*}{RT} + (1-x)\frac{\Delta h^*}{RT_f}\right] \tag{2}$$

$F(t)$ is the relaxation function of the given property, $t$ is time, $\tau$ is the relaxation time, $\beta$ is the non-exponentiality parameter ($0 < \beta \leq 1$), $A$ is the pre-exponential factor, $x$ is the non-linearity parameter ($0 < x \leq 1$), $\Delta h^*$ is the apparent activation energy of the structural relaxation, $R$ is the universal gas constant, $T$ is temperature and $T_f$ is the fictive temperature. The fictive temperature $T_f$ corresponds to the temperature of pseudo-equilibrium undercooled liquid with the same structure as is that of the described glass. The so-called reduced heat flow $\Phi^{red}$ representing the normalization of the DSC data in the glass transition region substitutes the relaxation function *F(t)* (see Eq. 3).

$$\Phi^{red} = \frac{\Phi(T)-\Phi_g(T)}{\Phi_l(T)-\Phi_g(T)} \tag{3}$$

where $\Phi(T)$ are the measured DSC data, while $\Phi_g(T)$ and $\Phi_l(T)$ are the temperature dependences extrapolated from the glassy and undercooled liquid regions, respectively. [22]

The kinetic analysis of structural relaxation data in the present work is based on data from the constant ratio (CR) cycles, where the sample is cyclically cooled and heated through $T_g$, cooling and heating rates vary during each cycle but the ratio between the consequent cooling and heating rates is always the same. In the first step of kinetic analysis of the relaxation data, the value of the apparent activation energy $\Delta h^*$ is determined [23]:

$$-\frac{\Delta h^*}{R} = \left[\frac{d\ln|q^-|}{d\,(1/T_p)}\right]_{\frac{q^-}{q^+}=const.} \tag{4}$$

where $T_p$ is the temperature of the maximum of the relaxation peak obtained during the heating scan and $q^-$ is the cooling rate applied during the preceding cooling step. Then, the remaining TNM parameters are determined from the curve-fitting procedure of the relaxation data obtained during the CR cycles. [19,21]

## 2.2 Cold crystallization

The kinetic analysis of DSC crystallization data may be realized by enumerating the basic kinetic equation (Eq. 5) [24]:

$$\Phi = \Delta H \cdot A \cdot e^{-\frac{E}{RT}} \cdot f(\alpha) \tag{5}$$

where $\Phi$ is the measured heat flow, $\Delta H$ is the crystallization enthalpy, $A$ is the pre-exponential factor, $E$ is the apparent activation energy of the studied process, $R$ is the universal gas constant, $T$ is the temperature and $f(\alpha)$ stands for an expression of a kinetic model with $\alpha$ being conversion.

The evaluation of the apparent activation energy of crystallization $E$ is the first step of kinetic analysis. In this regard the Kissinger [25] and Kissinger-Akahira-Sunose [26] methods are usually used for this task. These methodologies are expressed by the following equations:

$$ln\left(\frac{q^{+}}{T_p^2}\right) = -\frac{E}{RT_p} + const. \quad (6)$$

$$ln\left(\frac{q^{+}}{T_\alpha^{1.92}}\right) = -1.0008\frac{E}{RT_\alpha} + const. \quad (7)$$

where $T_p$ is the maximum of the crystallization peak, $q^{+}$ is the heating rate, $T_\alpha$ is the temperature corresponding to certain chosen values of conversion $\alpha$. The advantage of the iso-conversional KAS method lies in an estimation of $E$ for all involved sub-processes, because this equation provides the $\alpha$ dependence of $E$, in contrast to the Kissinger method, which provides information about the $E$ of the dominant process (the only value corresponding to the maximum of the largest peak). [25,26]

After the apparent activation energy is estimated, the next step of kinetic analysis proceeds with the finding of the most suitable kinetic model to describe the DSC crystallization data. In the present work the autocatalytic AC(M,N) [27] model was used to describe the DSC crystallization data. The model is expressed by Eq. 8, where the $M$ and $N$ parameters stand for the so-called kinetic exponents.

$$f(\alpha) = \alpha^M(1-\alpha)^N \quad (8)$$

The advantage of the autocatalytic model lies in higher flexibility to experimental kinetic data.

## 3. Experimental

Pure crystalline elements (5N, Sigma Aldrich) were used to prepare the $Ge_{20}Te_{75}I_5$ chalcogenide glass. A classical melt-quench technique in a rocking furnace was carried out; the first annealing was done at 500 °C (12 h), after that the furnace temperature was increased at 950 °C (24 h) and for the last 12 h the furnace temperature was decreased to 650 °C. The melt was quenched in cold water. The obtained glassy material was treated as follows; small

plates broken off from a thin glassy sheet formed inside the quenched ampoule were used as "bulk" samples (the sample average particle size was assigned $d_{aver}$ = 1 mm) - the main goal was to acquire samples with minimum of mechanical defects and heterogeneities. The main glassy ingot was thereafter crushed in an agate mortar and sifted through the sieves with defined mesh size; the following powder particle size fractions were obtained: 20-50, 50-125, 125-180, 180-250, 250-300, 300-500 μm.

The relaxation and crystallization behavior of prepared chalcogenide glass was studied by means of DSC using a Q2000 heat-flow calorimeter (TA Instruments) equipped with an autosampler, RCS90 cooling accessory and T-zero technology. The calibration of calorimeter was performed based on the melting temperatures of In, Zn and $H_2O$. The DSC cell was purged with a steady flow of dry nitrogen at 30 $cm^3 \cdot min^{-1}$. The masses of samples were approx. 8 mg; the hermetically sealed standard low-mass aluminum DSC pans were used. The DSC crystallization experiments were performed under the non-isothermal conditions; the powdered and bulk samples were studied. The samples were equilibrated at 50 °C and then heated to 400 °C. The applied heating rates $q^+$ were 0.5; 1; 2; 5; 10 and 20 $°C.min^{-1}$. For the enthalpy relaxation the samples were cycled between 50 and 175 °C; the employed CR cycles ratios were $q^+/q^-$ = 1 and 3; applied cooling rates were 0.5, 1, 2, 3, 5, 7, 10, 15, 20 and 30 $°C.min^{-1}$.

The XRD analysis was used to identify the crystalline phases of DSC-crystallized powdered samples and was performed using D8 Advance diffractometer (Bruker AXS, Germany) with Bragg-Brentano goniometer equipped with Ni-beta filter and LynxEye detector. The measurement was repeated 20 times and sum of the obtained diffraction patterns was obtained; total time per step was 312 s.

The Raman spectra were obtained by using the DXR2 Raman microscope (Thermo Fisher Scientific) utilizing 780 nm excitation laser (0.1 mW, 90 scans → 10 s each; laser spot

size equal to 3.1 μm) and CCD detector. The Raman spectra were collected from the freshly fractured bulk glasses and also from the DSC-crystallized samples. The verification of amorphous nature of glassy samples was done visually via the microscope and spectroscopically via the constant signal at prolonged exposure.

The infrared microscopy procedure was performed by infrared microscope Olympus BX51 equipped with XM10 camera used in the reflection mode. The samples for this procedure were prepared by heating the bulk samples in DSC to 223 °C and the quenching of samples followed (the applied heating rate was 5 °C.min$^{-1}$). The goal of microscopic study was the uncovering of the particular types of formed crystallites.

## 4. Results

In the following section, the basic thermal and structural information provided by DSC, XRD analysis, Raman spectroscopy and infrared microscopy will be presented. Thermal behavior of $Ge_{20}Te_{75}I_5$ chalcogenide glass was studied using DSC under non-isothermal conditions in the temperature interval 100-400 °C in dependence on particle size. The Fig. 1 illustrates the obtained DSC curves representing all studied particle size fractions and bulk samples measured at heating rates 1 °C.min$^{-1}$ (Fig. 1A) and 10 °C.min$^{-1}$ (Fig. 1B). The first apparent thermal effect on DSC curve corresponds to the glass transition, the position of this effect does not change with increased particle size. The glass transition effect shows an overshoot effect (relaxation peak), the maximum of which was used to determine the glass transition temperature $T_g$. The second observable effect on DSC curve is the exothermal peak corresponding to the crystallization process. As can be seen, the crystallization manifests a complex behavior with two well-distinguished sub-processes in case of the fine powders (fractions with particle size 20-50 and 50-125 μm); nonetheless in case of the coarser powders, the complexity becomes less obvious and the two sub-peaks start

to merge. The typical temperature shift of crystallization with applied heating rate $q^+$ (as a consequence of crystallization kinetics) is evident; also the crystallization temperature of bulk samples is shifted to higher temperatures compared to the powdered samples. The glass transition and crystallization effects are well separated (this is important for proper evaluation of the kinetic behavior of the particular phenomena, as will be shown later). Their mutual distance increases with applied heating rate and also with increasing particle size; the delay of the crystallization process in case of coarser powders or bulk samples is most probably caused by the lack of crystallization centers (as will be discussed in detail later). The last effect observable on the DSC curves is the melting peak. Its complex character clearly corresponds to simultaneous melting of different crystallization products. Also, as expected the extrapolated onset of the melting process was found to be not influenced by experimental conditions (particle size, $q^+$), which confirms the negligible effects of thermal gradients on the resulting measurements. For the purpose of identifying the crystallization processes and products, the XRD analysis, Raman spectroscopy and infrared microscopy were utilized.

The outcome from XRD analysis is displayed in Fig. 2A - the diffraction pattern of the fully crystallized $Ge_{20}Te_{75}I_5$ powder (particle size: 20-50 μm) is shown. The identified crystalline phases were: hexagonal tellurium (a = b = 4.45720, c = 5.92900; $\alpha = \beta = 90°$, $\gamma = 120°$), rhombohedral GeTe (a = b = 4.16160, c = 10.678; $\alpha = \beta = 90°$, $\gamma = 120°$) and cubic $GeI_4$ (a = b = c = 12.03030; $\alpha = \beta = \gamma = 90°$); the respective diffraction lines are in Fig. 2A indicated by empty and filled symbols. Akin diffraction patterns were obtained for materials containing $GeTe_4$ matrices doped with Se or Ga [13,14,28] and also for pure $GeTe_4$ [29], where the initial Te precipitation is followed by crystallization of GeTe and other crystalline phases corresponding to the presence of the respective dopant. In the Ge-Te-Se systems [13,28], some unidentified diffraction lines occur, probably corresponding to a minor crystalline phase consisting from distorted $GeTe(Se)_4$ tetrahedra; also under certain conditions

(low $q^+$, large bulk-to-surface ratio) the monoclinic $GeSe_2$ crystalline phase appeared. In case of the Ge-Ga-Te system [14], the $Ga_2Te_3$ (at higher temperatures also $Ga_2Te_5$) was identified as the accompanying crystalline phase.

Raman spectra of as-prepared (glassy) and crystalline samples are depicted in Fig. 2B, where the red-line Raman spectrum corresponds to the freshly fractured bulk glassy sample and the black-line Raman spectrum represents the DSC-crystallized sample. The spectra of glassy sample can be described using the following assignments: A (73 $cm^{-1}$) and B (92 $cm^{-1}$) ~ pure Te structures [30]; C (125 $cm^{-1}$) ~ the symmetric stretching mode of corner-sharing Te-rich $GeTe_4 - {}_nGe_n$ (n = 0, 1, 2) tetrahedra [31-33]; D (141 $cm^{-1}$) ~ the highly ordered Te structures [30,31,34]; E (154 $cm^{-1}$) ~ symmetric stretching mode of edge-sharing $GeTe_4$ (or Ge-rich) tetrahedral, or a contribution from short, amorphous, distorted Te chains [32,35-37]. The assignments for the bands in the DSC-crystallized sample spectrum are: A* (78 $cm^{-1}$) ~ crystalline Ge-Te vibrations [37,38]; B* (89 $cm^{-1}$) ~ crystalline Te-Te chains [38]; C* (120 $cm^{-1}$) ~ signals from crystalline Te [37,38]; D* (138 $cm^{-1}$) ~ crystalline Te-Te chains [38,39]; E* (170 $cm^{-1}$) ~ vibrations of edge-sharing $GeTe_{4-n}Ge_n$ units [38,39]. Comparing the two Raman spectra, significant increase of the highly ordered Te-structures can be observed for the crystallized sample, whereas the amount of corner-sharing Te-rich $GeTe_4 - {}_nGe_n$ (n = 0, 1, 2) tetrahedra decreases during crystallization.

Infrared microscopy procedure was performed in order to identify the crystallites forming in the $Ge_{20}Te_{75}I_5$ glass. In Figs. 2C and 2D, the micrographs of partially crystallized bulk samples are displayed; graph C shows a surface layer, graph D depicts a cross-sectional view of a fractured bulk sample. As can be seen, the predominant crystallization mechanism is the surface crystallization with crystallites growing inwards perpendicularly to the surface, but some volume-located crystallites are detected, too. In previous study dealing with the crystallization of pure $Ge_{20}Te_{80}$ [29], the strict surface crystallization was found. On the other

hand, the addition of some dopants (e.g. Se [13] or Ga [14]) leads to a change of the crystallization process, where the bulk-located crystallites start to manifest – in this respect the crystallization behavior of $Ge_{20}Te_{75}I_5$ looks similar to these Se- and Ga-doped $GeTe_4$ systems. This claim is also supported by the XRD and Raman data, which show similar results for all three various dopants (Se, Ga, I). Moreover, the change of crystallization mechanisms with the mentioned dopants appears to be similar, which will be discussed in the following section.

## 5. Discussion

### 5.1 Relaxation kinetics

The structural relaxation kinetics of the $Ge_{20}Te_{75}I_5$ glass was studied based on the two series of CR cyclical experiments, where the ratios between the cooling rates and consequent heating rates $q^+/q^-$ were set to 1 and 3, respectively. In the first step of the kinetic analysis the apparent activation energy of the glass transition process was determined based on Eq. 4 – see Fig. 3A for the two dependences corresponding to the two series of CR cycles (CR1 and CR3 stand for the two utilized $q^+/q^-$ ratios). The slopes of the two dependences are fairly similar, indicating the same value of $\Delta h^*$. However, in case of the CR3 data obtained at highest heating rates the dependence exhibits curvature, deviating from the linear course. This is a proof of the existence of thermal gradients within the system, that cause the lag between true evolution and reception of the heat flow signal. The data also show that up to the heating rate 30 °C·min$^{-1}$ no (or negligible) influence of thermal gradients occurs. This confirms the credibility of not only the present enthalpy relaxation data but also of the crystallization kinetics measurements, where heating rates up to 20 °C·min$^{-1}$ were used. The averaged slopes of the dependences depicted in Fig. 3A result in $\Delta h^* = 332.5 \pm 3.5$ kJ·mol$^{-1}$.

The evaluated activation energy was consequently used in the curve-fitting procedure based on the TNM model (Eqs. 1 and 2) – the input $\Delta h^*$ was set fixed whereas the other parameters were allowed to optimize. In Fig. 3B the example CR1 DSC heating scan (heating at 2 °C·min$^{-1}$ following cooling at 2 °C·min$^{-1}$) is shown. The empty red points correspond to the optimization residua, i.e. the difference between the experimental and calculated (theoretical) data. Appropriately scattered residua indicate high quality of the description in terms of the TNM model and that no major features of the depicted curve are omitted in the description. Description of the other CR1 heating scans was of similar quality. The values of TNM parameters resulting from the optimization were: $x = 0.43 \pm 0.04$, $\beta = 0.74 \pm 0.05$ and $\ln(A/s^{-1}) = 93.3 \pm 1$. If we compare these results to those obtained for the pure $GeTe_4$ matrix [40] ($\Delta h^* = 393$ kJ·mol$^{-1}$, $x = 0.74$, $\beta = 0.77$), the largest differences can be found for the $\Delta h^*$ and x parameters (note that these two parameters are very closely interlinked). The marked difference between the TNM parameters of the I-doped and pure $GeTe_4$ matrices can be explained on the basis of the existing structural differences. It was reported in [41] that for a $Ge_{20}Te_{73}I_7$ glass the iodine bonds exclusively to germanium and that the overall structure is composed of $GeTe_4$ and $GeTe_3I$ tetrahedra connected by Te-Te bonds. Since Te and I atoms are of practically same size, the main difference is associated with the I atom terminating the tetrahedra interconnection at that corner. This is the possible reason for the I-doped $GeTe_4$ glass exhibiting lower activation energy for the relaxation motions – the matrix is less interconnected hence lower amount of bonds needs to be broken/transformed. In accordance, the lower value of non-linearity parameter x (indicating larger dependence of relaxation times on the current structure of the glass) present for the I-doped $GeTe_4$ matrix can correspond to the lower interconnectivity, where possibly larger structural entities need to be moved in order to propagate the relaxation movement. As the structure on the molecular level is essentially the same and also the nature of the relaxation movements seems not to change, it is

understandable that the distribution of relaxation times remains similar (as expressed by similar value of the non-exponentiality parameter β).

5.2 Cold crystallization kinetics

In order to describe the crystallization kinetics occurring in case of $Ge_{20}Te_{75}I_5$ chalcogenide glass, the complex crystallization behavior needs to be addressed. Therefore the Fraser-Suzuki (FS) deconvolution procedure [42] was applied on DSC data (see Eq. 9).

$$y = a_0 exp\left[-ln2\left[\frac{\ln(1+2a_3\frac{x-a_1}{a_2})}{a_3}\right]^2\right] \quad (9)$$

The FS function represents a four-parameter function, where $a_0$, $a_1$, $a_2$, $a_3$ are parameters corresponding to the amplitude, position, half–width and asymmetry of the curve [42,43]. In Figs. 4A and 4B, the examples of deconvoluted DSC curves are illustrated; the solid line denotes the overall fit of the experimental data, points represent the experimental DSC data, and the dashed lines indicate the two deconvoluted crystallization mechanisms. As can be seen in Figs. 4A and 4B, the crystallization process complexity can be described by two overlapping peaks with akin asymmetry (both processes will be investigated in terms of the AC(M,N) kinetic model - see below). The two well-distinguished peaks are noticed in case of $q^+ = 1$ °C.min$^{-1}$ for the two finest powders, and in case of $q^+ = 10$ °C.min$^{-1}$ only for the most finest powder (particle size 20-50 μm) - the presence of well-differentiated overlapping processes slightly decreases with increasing particle size and increasing applied heating rate. Quite different behavior was observed for bulk samples. The presence of low-α shoulder can be detected for the coarser powders and slower heating rate, and also for the faster-heated bulk sample; while in case of the higher applied heating rate the high-α shoulder starts to manifest. Thus the large variability of the crystallization process with experimental conditions occurs (see Fig. 1); all of these phenomena can be explained on basis of the manifestation of

different crystallization mechanisms. As was mentioned in section 4, the initial Te precipitation is followed by the crystallization of GeTe units, and probably the volume-located crystals may occur, so the two crystallization mechanisms appear to compete against each other, but still the surface crystallization remains dominant (see the results from XRD analysis, Raman spectroscopy and IR microscopy). Note that similar behavior was observed also for the Se-doped $GeTe_4$ materials [14,15,28].

The deconvoluted DSC data were subject to kinetic analysis as follows. The kinetic analysis of crystallization data starts with determination of the apparent activation energy of crystallization as was mentioned in Theory section; the Kissinger and Kissinger-Akahira-Sunose (KAS) methods were used for this task. In Figs. 4C and 4D, the so-called Kissinger plots corresponding to the first and second deconvoluted peak are shown. Acceptable linearity of the $T_p$ evolution with heating rate and particle size indicates uniformity of individual (deconvoluted) crystallization processes, which confirms that there is one independent crystallization mechanism associated with each deconvoluted kinetic peak. In Fig. 5A, the apparent activation energies evaluated separately for the first and second deconvoluted peaks by the Kissinger and KAS methods are shown in dependence on average particle size. Whereas for most powder fractions the values of activation energies are more-or-less constant, several trends are apparent in Fig. 5A. Firstly, in case of finest powder the activation energy of the second ("bulk crystal growth") process is very high – this may be associated with the physical dispositions of the sample as the small size of powder grains does not provide the ample space for the volume-located crystallization and spatial restrains may lead to increased difficulty of the crystal growth initiation. As the powder grain size increases towards bulk sample, activation energy of the first process (surface precipitation of Te) also increases in correspondence with the lack of catalyzing factors (lower amounts of mechanically induced defects serving as nucleation/growth centers). On the other hand, the

second crystallization process occurring possibly in bulk exhibits E rather similar to coarse powders, which indicates that the two crystallization processes are independent.

The development of the overall crystallization enthalpy $\Delta H_c$ values in dependence on average particle size $d_{aver}$ is depicted in Fig. 5B (the red points illustrate the dependence of finest powder $\Delta H_c$ values on applied heating rate). As can be seen, the $\Delta H_c$ values slightly decrease with $d_{aver}$; this trend confirms [44,45] the above-mentioned assumptions that the powdered glasses include high portion of mechanically induced defects, which enhance the nucleation and/or crystal growth processes. The lower $\Delta H_c$ present for the lowest $q^+$ then indicates the importance of energy deliverance for the volume-located growth in case of the finest powder, where the slow heating favors the low-E process (surface growth in this case) and, consequently, the sample will not reach full crystallinity due to heavy spatial restraints further suppressing the volume growth. [22]

In regard to the kinetic description of the crystallization data, the autocatalytic AC(M,N) model (defined by Eq. 8) was found to be suitable due to its flexibility. The Fig. 5C displays the determined values of kinetic exponents M and N in dependence on average particle size; no significant changes of M and N parameters corresponding to each deconvoluted peak with $d_{aver}$ were observed, but these parameters exhibit a certain variation with applied heating rate (see the error bars associated with M and N values). This again confirms that the two crystallization sub-processes are independent from each other.

The performed DSC measurements provide the values of characteristic temperatures, such as the glass transition temperature $T_g$, the crystallization temperature $T_c$, and the melting temperature $T_m$. These parameters are crucial in a glass-forming-ability and glass-stability predictions of mentioned chalcogenide materials in regard to the potential real-life IR optics applications. In general practice, various methods can be implemented, including e.g. the so-called $\Delta T$ criterion ($\Delta T = T_c - T_g$) [13,46,47] or Hruby criterion [48], the benefit of which lies

in both easy evaluation and utilizing all three characteristic temperatures (which provides more accurate correlation with glass stability and glass-forming ability [49]). In the present work we have employed the Hruby criterion (see Eq. 10), which actually represents the ΔT range "normalized" by the $T_m$ - $T_c$ difference.

$$K_H = \frac{(T_c - T_g)}{(T_m - T_c)} \tag{10}$$

The calculated values of $K_H$ in dependence on experimental conditions (the particle size and heating rate) are for the $Ge_{20}Te_{75}I_5$ system shown in Fig. 5D. Note that temperatures corresponding to the respective peak onsets were utilized as $T_c$ and $T_m$. The relative variability with applied experimental conditions is evident. The lowest $K_H$ value ($K_H$ = 0.1571) was obtained in case of the finest powder (20 - 50 μm) and the applied heating rate $q^+$ = 1 °C.min$^{-1}$, which is naturally related to the sample form, where the presence of mechanically induced defects facilitates the crystallization and as was mentioned above, the crystallization starts on surface by the precipitation of tellurium. The highest $K_H$ value ($K_H$ = 0.6639) was obtained for the coarsest powder (300 - 500 μm) and $q^+$ = 20 °C.min$^{-1}$. The $K_H$ values representing the bulk samples vary between $K_H$ ~ 0.3669 - 0.6062. The present results show that the glass stability evaluated via the simple three-temperature criteria can massively depend on the actual conditions of the DSC measurement and it is therefore crucial to specify these conditions for each such evaluation. It should be also noted that these criteria (based only on the DSC data) do not take into account e.g. the influence of materials viscous flow [50] and as such should be used only as a rough estimation.

## 6. Conclusions

Thermal behavior of the $Ge_{20}Te_{75}I_5$ chalcogenide glass was studied by means of DSC, XRD, Raman spectroscopy and infrared microscopy. The glass transition kinetics was

described in terms of the TNM model – the addition of iodine into the $Ge_{20}Te_{80}$ matrix was found to result in markedly smaller activation energy of the relaxation movements and also in higher non-linearity of the involved processes, decreasing the temperature-dependent behavior at the expense of the thermal history influence. Based on the structural information (the I atoms are reported to terminate the $GeTe(I)_4$ tetrahedra interconnections at that corners), the relaxation kinetics was interpreted in terms of the decreased interconnectivity of the Ge-Te-I glassy matrix. Concerning the crystallization behavior, mathematic deconvolution was used to separate the particular crystal growth sub-mechanisms contributing to the overall crystallization process. Full-scale kinetic study was performed to investigate the trends in kinetic parameters. The combined results from DSC and XRD revealed that the crystallization starts with surface precipitation of Te, being followed by formation of the GeTe and $GeI_4$ phases, both at the surface and in volume of the glassy material. Presence of mechanically induced defects significantly accelerates the crystallization (the Te precipitation in particular). This in consequence largely influences the results provided by glass stability criteria.

**Acknowledgements**

This work has been supported by the Czech Science Foundation under project No. 17-11753S.

**References**

[1] P. Lucas, G.J. Coleman, S. Jiang, T. Luo, Z. Yang, Opt. Mater. 47 (2015) 530.
[2] S. Hocdé, C. Boussard-Plédel, G. Fonteneau, J. Lucas, Solid State Sci. 3 (2001) 279–284.
[3] S. Maurugeon, B. Bureau, J. Lucas, J. Non-Cryst. Solids 355 (2009) 2074–2078.
[4] A.A. Wilhelm, C. Boussard-Pledel, P. Lucas, Proc. SPIE 6433 (2007) 1–8.
[5] P. Houizot, C. Boussard-Pledel, A.J. Faber, L. Cheng, B. Bureau, P.A. Nijnatten, W. Gielesen, J. Pereira, J. Lucas, Opt. Exp. 15 (2007) 12529–12538.
[6] A. Léger, Adv. Space Res. 25 (2000) 2209.
[7] S. Cui, R. Chahal, C. Boussard-Plédel, V. Nazabal, J.L. Doualan, J. Troles, J. Lucas, B. Bureau, Molecules 18 (2013) 5373-5388.

[8] C. Conseil, V.S. Shiryaev, S. Cui, C. Boussard-Pledel, J. Troles, A.P. Velmuzhov, A.M. Potapov, A.I. Suchkov, M.F. Churbanov, B. Bureau, J. Lightwave Technol. 31 (2013) 1703-1707.
[9] C. Cheng, X.S. Wang, T.X. Fu, X.H. Zhang, Guangzi Xuebao/Acta Photonica Sinica 44 (2015) 0216002.
[10] G. Wang, Q. Nie, X. Wang, S. Dai, T. Xu, X. Shen, X. Zhang, Phys. B 405 (2010) 4424-4428.
[11] G. Wang, Q. Nie, M. Barj, X. Wang, S. Dai, X. Shen, T. Xu, X. Zhang, J. Phys. Chem. Sol. 72(2011) 5-9.
[12] P. Petkov, V. Ilcheva, D. Wamwangi, M. Wuttig, P. Ilchev, T. Petkova, J. Optoelectron. Adv. M. 11 (2009) 1261-1264.
[13] R. Svoboda, D. Brandová, J. Málek, J. Alloys Compd. 680 (2016) 427-435.
[14] R. Svoboda, D. Stříteský, Z. Zmrhalová, D. Brandová, Jiří Málek, J. Non-Cryst. Solids 445–446 (2016) 7–14.
[15] R. Svoboda, D. Brandová, J. Málek, J. Non-Cryst. Solids 432 (2016) 493-498.
[16] S. Danto, P. Houizot, C. Boussard-Pledel, X.H. Zhang, F. Smektala, J. Lucas, Adv. Funct. Mater. 16 (2006) 1847.
[17] P. Petkov, V. Ilcheva, D.Wamwangi, M.Wuttig, P. Ilchev, T. Petkova, J. Optoelectron. Adv. Mater. 11 (2009) 1261.
[18] J. Sun, Q. Nie, X.S. Wang, S. Dai, X. Zhang, B. Bureau, C. Boussard, C. Conseil, H. Ma, Infrared Phys. Technol. 55 (2012) 316-319.
[19] A.Q. Tool, J. Am. Ceram. Soc., 29 (1946) 240–253.
[20] O.S. Narayanaswamy, J. Am. Ceram. Soc., 54 (1971) 491–497.
[21] C.T. Moynihan, A.J. Easteal, M.A. DeBolt, J. Tucker, J. Am. Ceram. Soc., 59 (1976) 12-16.
[22] R. Svoboda, J. Málek, J. Non-Cryst. Solids 378 (2013) 186.
[23] R. Svoboda, J. Therm. Anal. Calorim. 121 (2015) 895.
[24] J. Málek, J. Klikorka, J. Therm. Anal. 32 (1987) 1883.
[25] H.E. Kissinger, Anal. Chem. 29 (1957) 1702.
[26] M.J. Starink, Thermochim. Acta 404 (2003) 163.
[27] J. Šesták, Thermophysical Properties of Solids, Their Measurements and Theoretical Analysis, Elsevier, Amsterdam, 1984.
[28] D. Brandová, R. Svoboda, J. Málek, J. Non-Cryst. Solids 433 (2016) 75-81.
[29] R. Svoboda, D. Brandová, J. Málek, J. Therm. Anal. Calorim. 123 (2016) 195-204.
[30] E.M. Vinod, A.K. Singh, R. Ganesan, K.S. Sangunni, J. Alloys Compd. 537 (2012) 127-132.
[31] S.S. Garje, M.C. Copsey, M. Afzaal, P.O. Brian, T. Chivers, J. Mater. Chem. 16 (2006) 4542.
[32] R. De Bastiani, E. Carria, S. Gibilisco, M.G. Grimaldi, A.R. Pennisi, A. Gotti, A. Pirovano, R. Bez, E. Rimini, Phys. Rev. B 80 (2009) 245205.
[33] K.S. Andrikopoulos, S.N. Yannopoulos, G.A. Voyiatzis, A.V. Kolobov, M. Ribes, J. Tominaga, J. Phys. Condens. Matter 18 (2006) 965.
[34] A.S. Pine, G. Dresselhaus, Phys. Rev. B 4 (1971) 356.
[35] O. Uemura, N. Hayasaka, S. Tokairin, T. Usuki, J. Non-Cryst. Solids 205 (1996) 189.

[36] M. Upadhyay, S. Murugavel, M. Anbarasu, T.R. Ravindran, J. Appl. Phys. 110 (2011) 083711.
[37] M.H. Brodsky, R.J. Gambino, J.E. Smith, Y. Yacoby, Phys. Status Solidi B 52 (1972) 609.
[38] E.M. Vinod, K.S. Sangunni, Thin Solid Films 550 (2014) 569-574.
[39] A.V. Kolobov, P. Fons, J. Tominaga, A.L. Ankudinov, S.N. Yannopoulos, K.S. Andrikopoulos, J. Phys. Condens. Matter. 16 (2004) 5103.
[40] R. Svoboda, J. Málek, J. Non-Cryst. Sol. 422 (2015) 51-56.
[41] P. Jóvari, I. Kaban, B. Bureau, A. Wilhelm, P. Lucas, B. Beuneu, D. A. Zajac, J. Phys. Condens. Matter 22 (2010) 404207.
[42] A. Perejón, P.E. Sánchez-Jiménez, J.M. Criado, L.A. Pérez-Maqueda, J. Phys. Chem. B 115 (2011) 1780.
[43] R. Svoboda, J. Málek, J. Therm. Anal. Calorim. 119 (2015) 155.
[44] R. Svoboda, J. Málek, J. Therm. Anal. Cal. 115 (2014) 81.
[45] R. Svoboda, J. Málek, J. Alloys Compd. 81 (2015) 101–108.
[46] S. Danto, P. Houizot, C. Boussard-Pledel, X.-H. Zhang, F. Smektala, J. Lucas, Adv. Funct Mater. 16 (2006) 1847–52.
[47] G. Wang, C. Li, Q. Nie, Z. Pan, M. Li, Y. Xu, et al., J. Non-Cryst Solids 463 (2017) 80-84.
[48] A. Hrubý, Czech J Phys B. 22 (1972) 1187–1193.
[49] L. F. M. Nascimento, N. O. Dantas, Mater. Lett. 61 (2007) 912.
[50] R. Svoboda, D. Brandová, M. Chromčíková, M. Liška, J. Alloys. Compd. – submitted.

**Figure captions**

Figure 1: Example DSC curves measured at a heating rates 1 and 10 °C·min$^{-1}$ for the all studied particle size fractions and bulk samples (graphs A and B). Exothermic effects evolve in the "upwards" direction.

Figure 2: A) XRD diffraction patterns of the partially (the first crystallization peak) and fully crystallized $Ge_{20}Te_{75}I_5$ material.
B) Raman spectra of as-prepared (glassy) and crystalline samples; compositional evolution of the spectra is suggested by the respective symbols.
C), D) The IR micrographs of partially crystallized bulk samples; graph C - a surface layer, graph D - a cross-sectional view of a fractured bulk sample.

Figure 3: A) The determined apparent activation energy of the glass transition process for the two dependences corresponding to the two series of CR cycles (CR1 and CR3 stand for the two utilized $q^+/q^-$ ratios); the depicted averaged slopes of the dependences result in $\Delta h^* = 332.5 \pm 3.5$ kJ·mol$^{-1}$.
B) The example CR1 DSC heating scan (heating at 2 °C·min$^{-1}$ following cooling at 2 °C·min$^{-1}$).

Figure 4: A), B) The examples of deconvoluted DSC curves obtained for the powder fractions with particle size 20-50 μm (A) and 300-500 μm (B) and the applied heating rates 1 and 20 °C.min$^{-1}$.
C), D) The so-called Kissinger plots corresponding to the first and second deconvoluted peak for all studied particle size fractions and bulk samples.

Figure 5: A) The evaluated apparent activation energies separately for the first and second deconvoluted peaks by the Kissinger and KAS methods in dependence on average particle size.
B) The development of the overall crystallization enthalpy $\Delta H_c$ values in dependence on average particle size $d_{aver}$; the red points illustrate the dependence of finest powder $\Delta H_c$ values on applied heating rate.
C) The determined values of kinetic exponents M and N in dependence on average particle size.
D) The calculated values of $K_H$ in dependence on experimental conditions (the particle size and heating rate).

Fig1

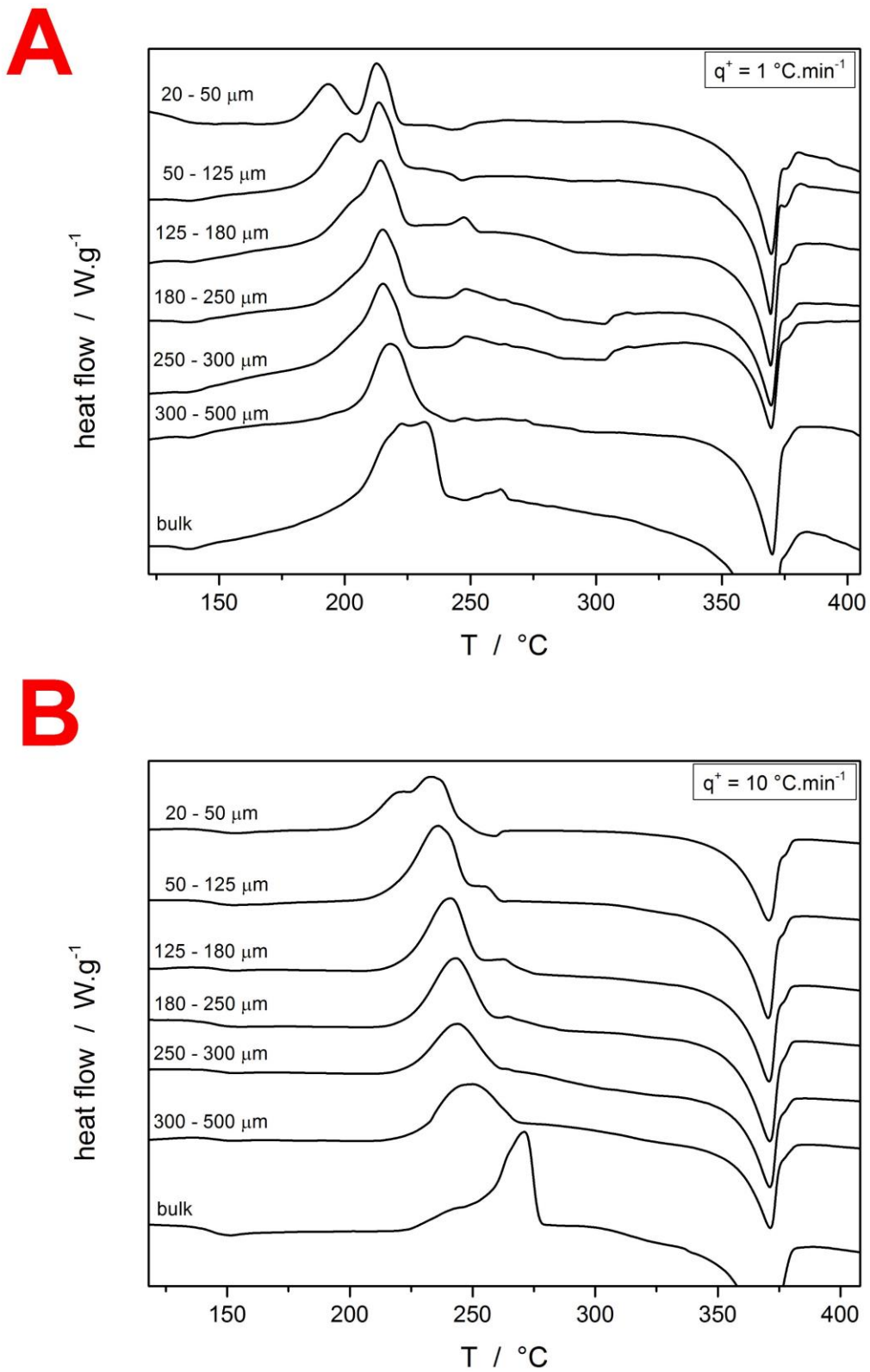
A
q+ = 1 °C.min-1
20 - 50 µm
50 - 125 µm
125 - 180 µm
180 - 250 µm
250 - 300 µm
300 - 500 µm
bulk
heat flow / W.g-1
150
200
250
300
350
400
T / °C
B
q+ = 10 °C.min-1
20 - 50 µm
50 - 125 µm
125 - 180 µm
180 - 250 µm
250 - 300 µm
300 - 500 µm
bulk
heat flow / W.g-1
150
200
250
300
350
400
T / °C

Fig 2

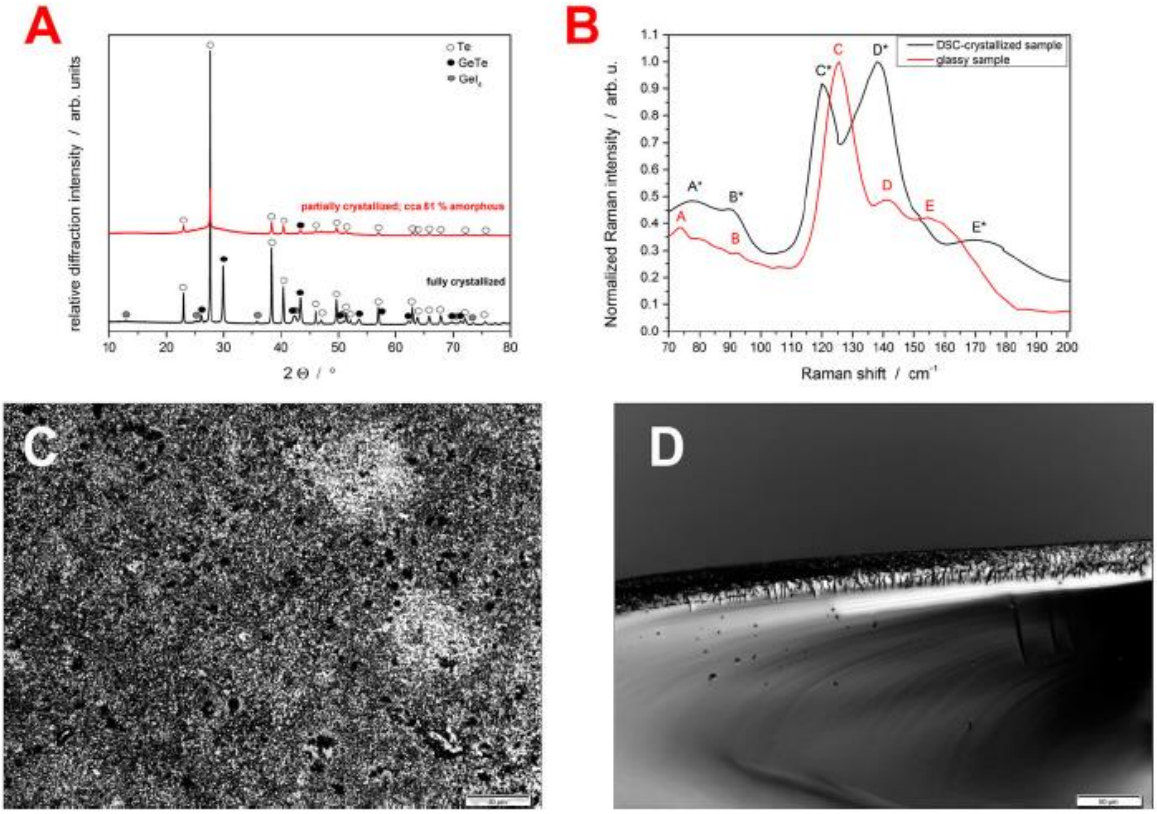
A
relative diffraction intensity / arb. units
Te
GeTe
GeI4
partially crystallized; cca 51 % amorphous
fully crystallized
2 Θ / °
B
Normalized Raman intensity / arb. u.
DSC-crystallized sample
glassy sample
A*
B*
C*
D*
E*
A
B
C
D
E
Raman shift / cm-1
C
D

Fig 3

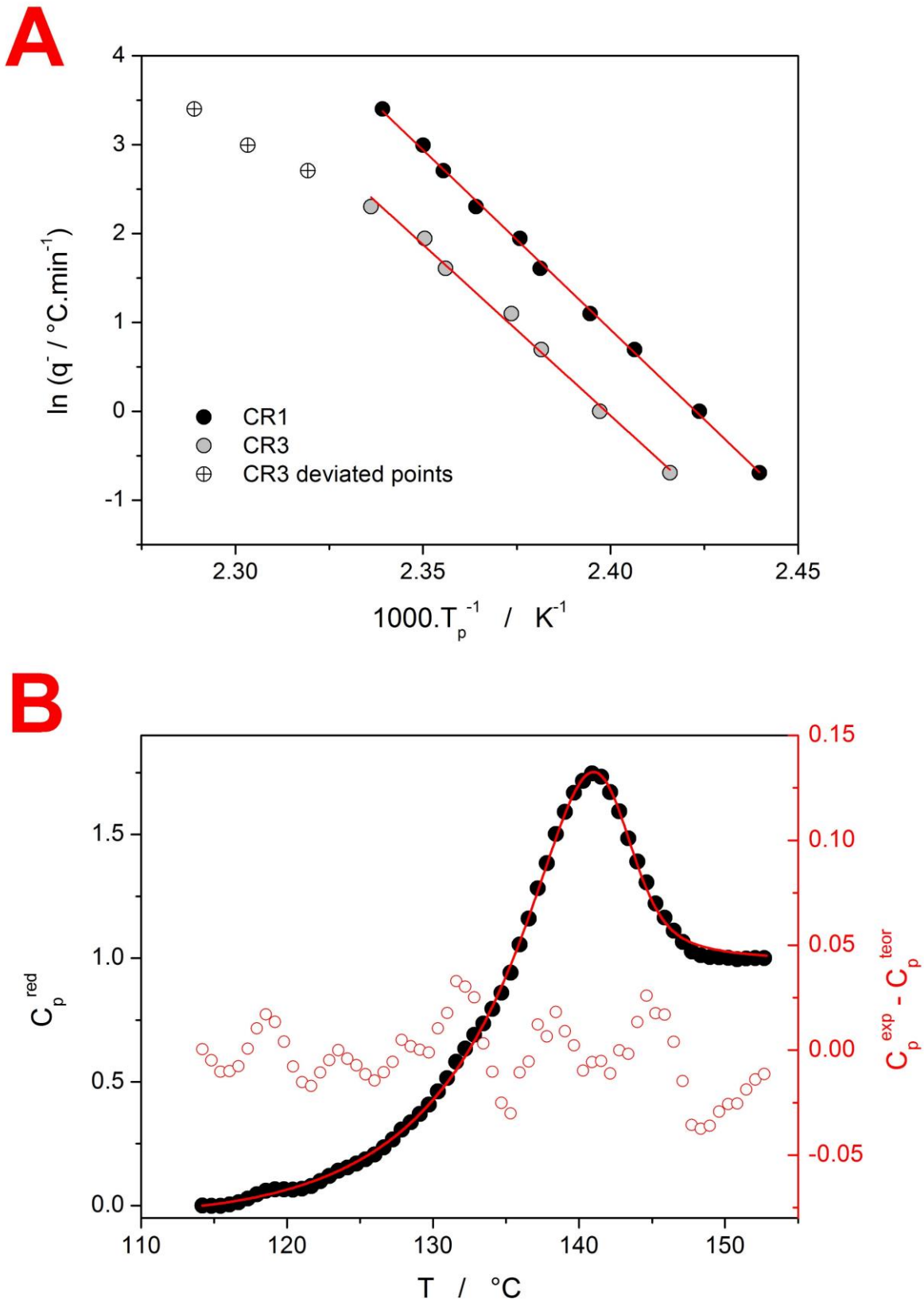
A
4
3
2
1
0
-1
ln (q- / °C.min-1)
CR1
CR3
CR3 deviated points
2.30
2.35
2.40
2.45
1000.Tp-1 / K-1
B
1.5
1.0
0.5
0.0
Cp red
0.15
0.10
0.05
0.00
-0.05
Cp exp - Cp teor
110
120
130
140
150
T / °C

Fig 4

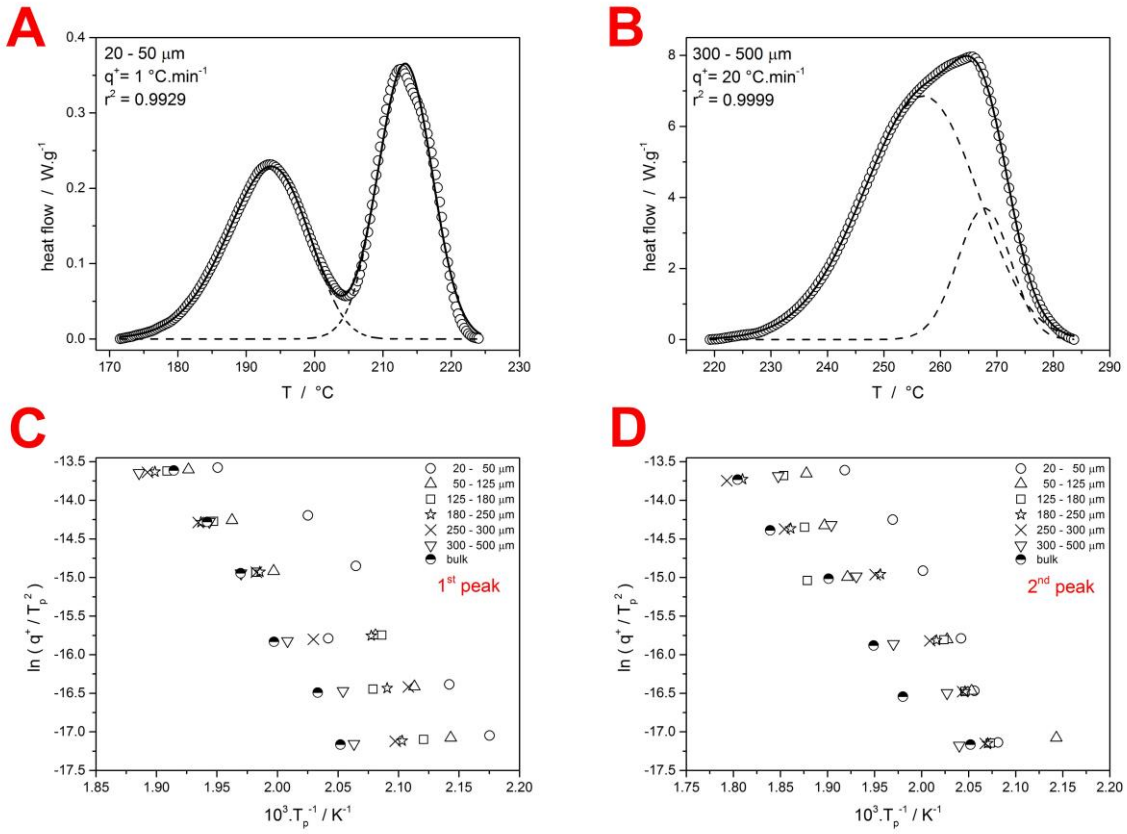
A
20 - 50 μm
q+= 1 °C.min-1
r2 = 0.9929
heat flow / W.g-1
T / °C
B
300 - 500 μm
q+= 20 °C.min-1
r2 = 0.9999
heat flow / W.g-1
T / °C
C
20 - 50 μm
50 - 125 μm
125 - 180 μm
180 - 250 μm
250 - 300 μm
300 - 500 μm
bulk
1st peak
ln ( q+ / Tp2 )
10³.Tp-1 / K-1
D
20 - 50 μm
50 - 125 μm
125 - 180 μm
180 - 250 μm
250 - 300 μm
300 - 500 μm
bulk
2nd peak
ln ( q+ / Tp2 )
10³.Tp-1 / K-1

Fig 5

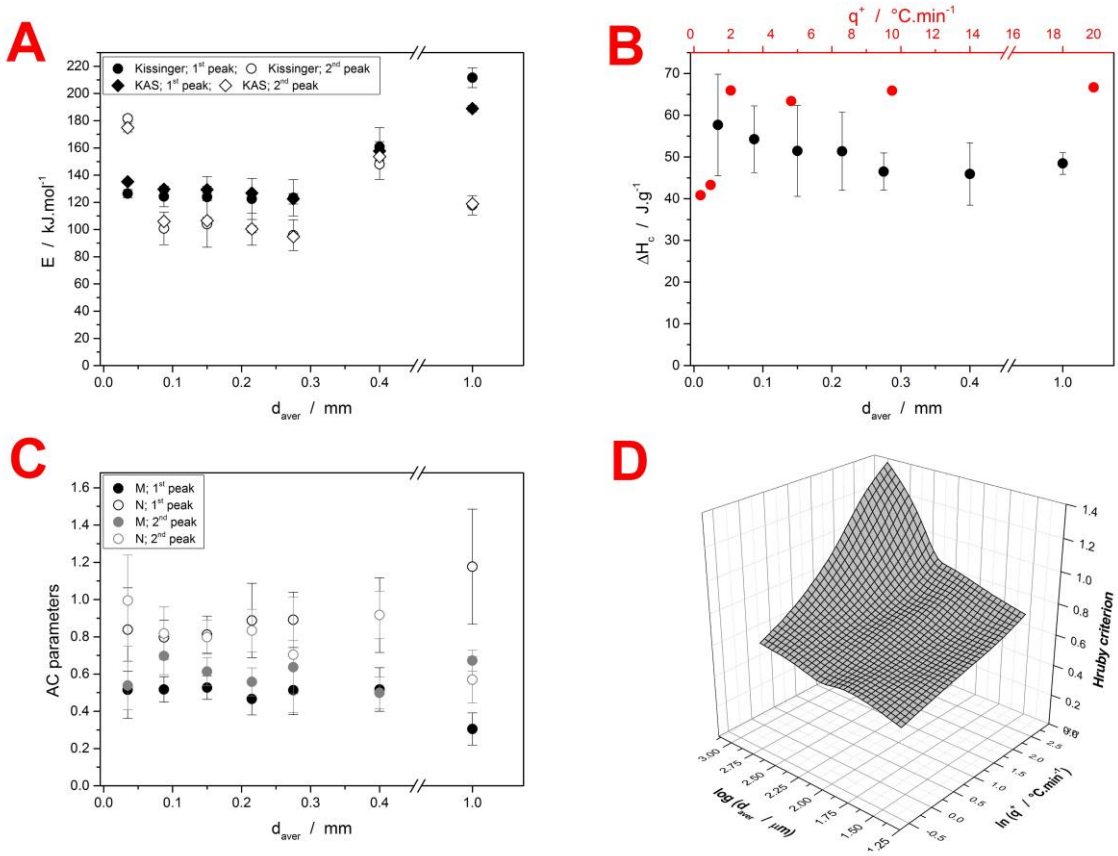
A
Kissinger; 1st peak; Kissinger; 2nd peak
KAS; 1st peak; KAS; 2nd peak
E / kJ.mol-1
daver / mm
B
q+ / °C.min-1
ΔHc / J.g-1
daver / mm
C
M; 1st peak
N; 1st peak
M; 2nd peak
N; 2nd peak
AC parameters
daver / mm
D
Hruby criterion
log (daver / μm)
ln (q+ / °C.min-1)